Marine vertical gravity gradients reveal the global distribution and tectonic significance of "seesaw" ridge propagation

Hugh Harper[1], Brook Tozer[1], David T. Sandwell[1] and Richard N. Hey[2]

[1]Institute of Geophysics and Planetary Physics, Scripps Institution of Oceanography, La Jolla, CA

[2]Hawaii Institute of Geophysics and Planetology, School of Ocean and Earth Science and Technology, University of Hawaii at Manoa, Honolulu, HI

Corresponding author: Hugh Harper (huharper@ucsd.edu)

Key Points:

- The process of "seesaw" ridge propagation is ubiquitous on seafloor that forms at half spreading rates between 10–40 mm yr^{-1}
- Globally, the total length of seesaw propagators is ~ 1/3 that of fracture zones
- Driving mechanisms previously proposed to explain unidirectional ridge propagation fail account for the behavior of seesaw propagators

This article has been accepted for publication and undergone full peer review but has not been through the copyediting, typesetting, pagination and proofreading process, which may lead to differences between this version and the Version of Record. Please cite this article as doi: 10.1029/2020JB020017.

Abstract

The segmentation of mid-ocean ridges is a defining characteristic of seafloor spreading, yet some tectonic processes operating at segment boundaries remain poorly understood. Here, we analyze new satellite-derived vertical gravity gradient (VGG) data, which reveal an abundance of off-axis seafloor features that are oblique to ridges and transform faults and thus reflect the occurrence of ridge propagation at some segment boundaries. However, unlike many propagating ridges, these features commonly reverse direction leaving W-shaped signatures in the seafloor which we refer to as "seesaw propagators" (SSPs). Using the VGG, we have documented these globally and find that: (1) SSPs are ubiquitous on seafloor that formed at half spreading rates between 10–40 mm yr^{-1} and their total length is about 1/3 that of fracture zones. (2) The lithospheric age offset across SSPs (0–2.5 Ma) is less than transform faults (2–10 Ma), which likely reflects a rheological threshold, whereby only young and weak lithosphere allows for "non-rigid" SSP behavior. (3) Isostatic modelling of well-surveyed SSPs confirms that they formed on young and thin (3 km) lithosphere. (4) The directional changes of SSPs in both time and space appear largely uncorrelated and cannot be explained by previous regional-scale models invoked to explain unidirectional ridge propagation and thus require a different driving force.

1 Introduction

Segmentation of the global mid ocean ridge (MOR) system is one of the most prominent features of the ocean floor, yet many details regarding the tectonic processes that occur at the segment discontinuities remain poorly understood. Transform faults are the most obvious form of ridge discontinuity, exhibiting large lateral offsets (> 30 km) of the ridges (Wilson, 1965); because they are stable in time and space, they produce the pronounced off-axis fracture zones that record the spreading motion of the plates. Along both slow (e.g. Sempere et al., 1990) and fast spreading ridges (e.g. Macdonald et al., 1988) there also exist smaller-scale, and less stable forms of ridge discontinuity. These features became apparent once detailed bathymetric and magnetic surveying of the ridges began (Schouten and White, 1980), after which, the prevalence and wide variety of ridge discontinuities was quickly recognized (Macdonald et al., 1991), including stable transform faults, propagating ridges (also known as rifts, Hey et al., 1986), overlapping spreading centers (Macdonald et al., 1988), and even smaller-scale discontinuities (Macdonald et al., 1991), including deviation in ridge axis linearity, changes in ridge petrology (Langmuir et al., 1986), and disruptions in the continuity of the magma lens (Kent et al., 1990). A thorough review of ridge segmentation can be found in Carbotte et al., (2015).

As these features continued to be discovered, it soon became apparent that the overall morphology of ridges and the style of their segmentation are intrinsically related to the seafloor spreading rate, and hence, the thermal structure and strength of the oceanic plates (e.g., Macdonald, 1982; Macdonald et al., 1987; Small and Sandwell, 1989; Chen & Morgan, 1990; Phipps-Morgan & Chen, 1993; Small & Sandwell, 1994; Dunn, 2015). Such variations include, for example, the presence of an axial valley or axial high, changes in the along strike spacing and ridge-to-ridge width of transform faults, and the presence of ridge propagation or microplate development (e.g., Hey et al., 1995). Several authors (Small and Sandwell, 1994; Chen and Morgan, 1990; Malinverno, 1991) have proposed that a major transition in the style of MOR tectonics occurs over the half spreading rate range of ~ 25-40 mm yr^{-1}. At rates lower than this (i.e., intermediate- to slow-spreading), the ridges are characterized by axial valleys and transform

faults and fracture zones have prominent troughs that are typically spaced ~ 50–80 km apart. Conversely, at higher spreading rates (i.e., fast-spreading) the ridge axis has an axial high, the transform faults are more widely spaced along axis (~100–1000 km) and the fracture zones have both ridges and troughs with smaller amplitudes.

The process of ridge propagation has been documented at all spreading rates with the exception of ultraslow spreading centers (e.g., Hey et al., 1986; Phipps-Morgan & Sandwell, 1994; Korenaga & Hey, 1996; Dannowski et al., 2011; Zheng et al., 2019). Ridge propagators were originally characterized by Hey (1977) who observed the off-axis V-shaped pseudofault pairs in marine magnetic anomalies. Figure 1a shows a schematic for a typical propagating ridge (PR). There is a small transform-like offset in the spreading ridge, which, over time, "migrates" parallel to the ridge leaving behind a pseudofault on the left (P1 in the figure). This "outer" pseudofault represents a small age offset (~ 1 Ma) in the seafloor and has a topographic expression that resembles that of a fracture zone. On the right is a broader sheared zone, bounded by the "inner" pseudofault and failed rift, that consists of crust that originally formed on the left plate and was transferred to the right plate. This transfer produces a sheared zone (S1 in the figure) having a width that is equal to the offset of the transform. The morphology of the sheared zone is wider and more complex than the outer pseudofault and thus one can distinguish between the outer pseudofault and sheared zone in the seafloor morphology.

Along slow- and intermediate-spreading ridges, there exists a unique but poorly documented type of propagating offset. These behave similarly to PRs but produce distinctive W-patterns in the ridge flanks (e.g. Figure. 1c). These features have previously been referred to as "discordant zones" (Grindlay et al., 1991) and "non-transform discontinuities" (NTDs) (e.g., Rea, 1978; Hey et al., 1980; Hey et al., 1986; McKenzie, 1986; Macdonald et al., 1988) but few have been mapped off axis at high resolution using multibeam sonar (e.g. Grindlay et al., 1991; Cochran and Sempere, 1997). A recent study by Zheng et al. (2019) examined the long-term evolution of NTDs. They found NTDs show structures typical of rift propagation (inner and outer pseudofaults) and crustal blocks transferred between ridge flanks by discontinuous jumps of the propagating ridge tip. The main difference between NTDs and the propagators found at higher spreading rates is that the rate of propagation is highly variable and the direction of propagation eventually reverses (e.g. Figure 1 and Figure 1 of Zheng et al., 2019). Short reversals in propagation direction have also been observed at PRs at faster spreading ridges and have been dubbed "dueling propagators" (Macdonald et al., 1988; Macdonald et al., 1992; Johnson et al., 1983; Wilson, 1990). Because—as we document in this paper—such features now appear so ubiquitous in the VGG at slow and intermediate spreading regimes, we have adopted the term "seesaw propagators" (SSPs) to describe these NTDs. We refer to off-axis features as "fossil" SSPs and the discontinuities at which they arise as NTDs or "active" SSPs.

In our more global analysis, we follow the recent terminology of Zheng et al., (2019) and refer to NTDs within a propagating ridge framework. Their detailed analysis of a region of the Mid-Atlantic Ridge between 24 and 27.5 N uses multibeam bathymetry, marine magnetic anomalies, and satellite-derived gravity to document the traces and age offsets of the NTDs. They find that all the NTDs are consistent with the propagating rift model where propagation usually occurs in discrete steps (i.e., the discontinuous propagation model of Hey et al., 1986).

They noted several differences between the detailed propagation mechanism of NTDs in slower spreading crust as compared with the model developed at intermediate and fast spreading ridges. First, because the slower spreading rift tips abut relatively cold lithosphere, propagation is restricted to where the crust is relatively thin and the shallower than normal mantle is likely to be weakened by serpentinization from seawater penetration. Second, the slower spreading rift has a 20-30 km wide rift valley that can accommodate lateral jumps in the rift axis. They conclude that that their model of NTDs has all the fundamental features of the standard propagating rift model. Our more global analysis does not usually include such high-resolution data, so we adopt the conclusions of the Zheng et al., (2019) study and assert the off-axis traces of all NTDs reflect a different style of rift propagation.

Some of the features included in our new global catalogue were included in the previous regional/global compilations of Phipps-Morgan & Sandwell, (1994), Briais and Rabinowicz (2002), and Matthews et al., (2011), who, in lieu of bathymetry data, used satellite-derived vertical gravity gradient (VGG) maps to identify these features. Since these studies, the amount and quality of satellite altimetry data has increased substantially, thus improving the accuracy and resolution of the global free-air gravity and VGG grids (Sandwell et al., 2019). The newest gravity grid has a spatial resolution of about 16 km compared to a resolution of 22 km in the grid used by Matthews et al., (2011) (Sandwell et al, 2019). In this study, we take advantage of these improvements (e.g., Figure 2) to analyze SSPs globally. Our study comprises five components:

(1) We use the new VGG maps to identify and digitize SSP pairs. Many of these are refined digitizations of features identified by Matthews et al., (2011). Though many were classified broadly as discordant zones, we categorize them as NTD/SSPs, and we also added previously unidentified SSPs. We use 224 features (112 pairs) identified by Matthews et al. (2011), many of which we have modified to fit new VGG maps. We identify an additional 146 features (73 pairs), for a total 370 SSPs (185 pairs), most of which are located in the Atlantic and Indian Ocean basins.

(2) We quantify the range of spreading rates where we observe this style of propagation and determine the range of age offsets across the ridge discontinuities as compared with transform faults.

(3) We investigate the detailed morphology and isostatic compensation of off-axis SSPs using high-resolution multibeam bathymetric data collected as part of the search for the missing Malaysia Airlines Flight 370 (MH370). This shows these off-axis features are isostatically compensated by locally thinned crust in agreement with Zheng et al., (2019).

(4) We demonstrate that traces of SSPs are symmetric about the ridge such that propagation direction reversals can be used as a new data type for detailed plate reconstructions.

(5) Finally, we test the validity of models previously proposed to explain the direction of propagation for unidirectional propagators for the case of seesaw propagation.

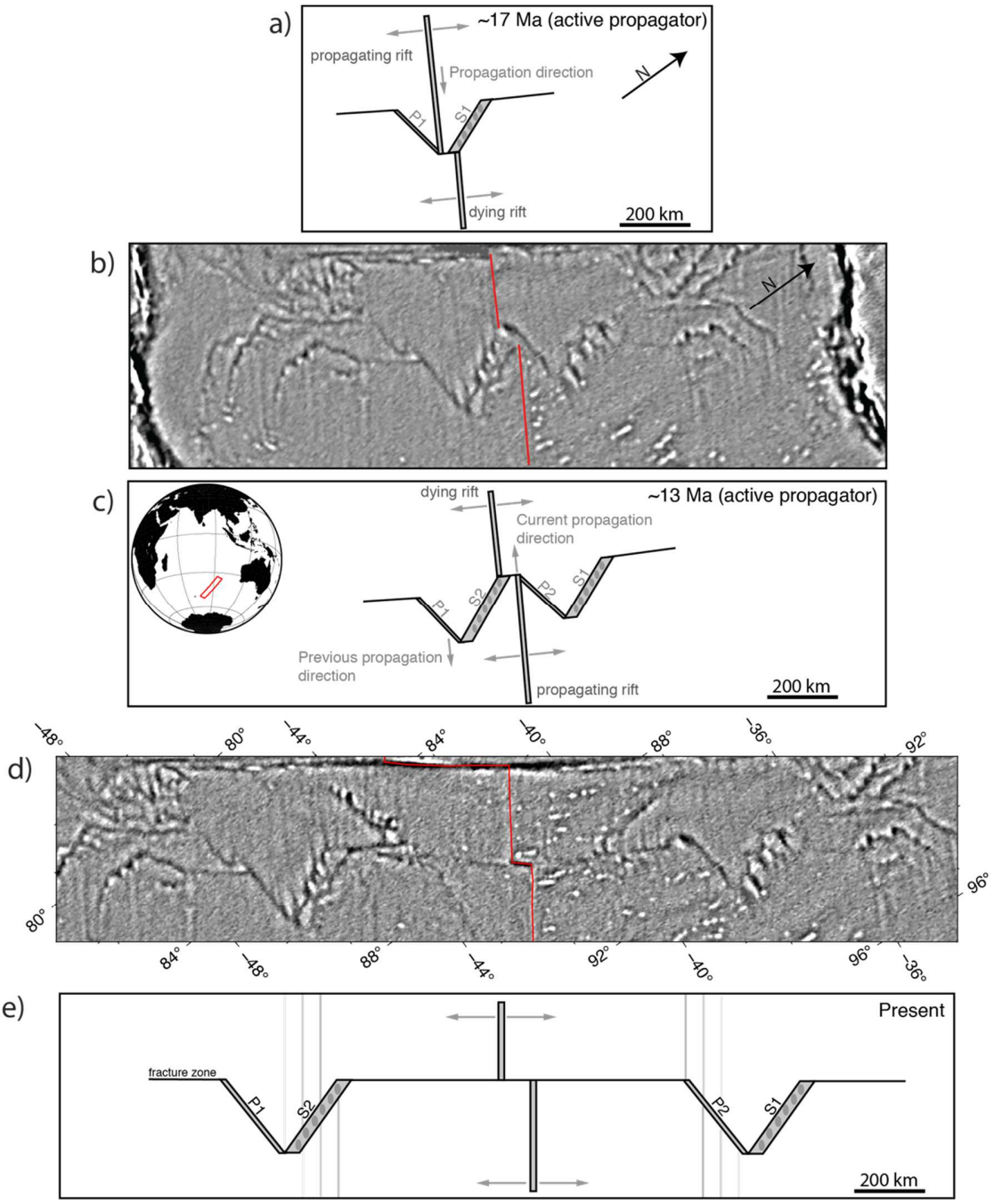

Figure 1. Evolution of a seesaw propagator in the Southeast Indian Ocean. The vertical gravity gradient (VGG) is rotated so ridges are up-down and transforms are left-right. (a) Reconstruction of VGG at 17 Ma shows the "outer" pseudofault (P1 left) and sheared zone (S1 right) of an ordinary eastward propagating ridge. The outer pseudofault has a straight trough while the sheared zone has a series of rotated blocks (i.e., the discontinuous propagation model of Hey et al., 1986). (b-c) The direction of propagation reverses resulting in a W-shaped scar in the VGG

at 13 Ma. (d-e) The transform offset increases by asymmetric spreading which stops ridge propagation resulting in an ordinary fracture zone with symmetrical V's at the distal ends. A seesaw propagator has one or more reversals in the direction of propagation.

2. Data

2.1 Marine vertical gravity gradient

To identify and digitize SSPs globally, we primarily used the VGG grid version 29 (v29). Details regarding the acquisition of these data and derivation of the gridded global map can be found in previous papers (e.g., Sandwell et al., 2019).

The VGG is $g_z(\boldsymbol{x}) = \partial g(\boldsymbol{x})/\partial z$, where $\boldsymbol{x}$ is the horizontal position vector. The VGG is used to highlight the shorter wavelength variations in the gravity field (e.g., Wessel and Lyons, 1997), that are better suited to mapping relatively fine-scale seafloor tectonic structures. In practice, the VGG is the curvature of the ocean surface as measured by satellite altimetry. The geoid height N, which is equal to the height of the ocean surface above the reference ellipsoid, is related to the gravitational potential U by Brun's formula $N = U/g_0$ where g_0 is the average acceleration of gravity. The potential satisfies Laplace's equation $\frac{\partial^2 U}{\partial x^2} + \frac{\partial^2 U}{\partial y^2} + \frac{\partial^2 U}{\partial z^2} = 0$ and the vertical gravity gradient is $g_z = -\frac{\partial^2 U}{\partial z^2}$, so $g_z = g_0\left(\frac{\partial^2 N}{\partial x^2} + \frac{\partial^2 N}{\partial y^2}\right)$. Unfortunately, by taking this derivative, the signal of the short wavelength background noise (predominantly from ocean waves) is also amplified. Improvements in the accuracy and spatial resolution of the VGG—owing to the inclusion of a wealth of new data obtained over the past eight years from altimeters CryoSat-2, Jason-1/2, and the first non-repeat Ka-band altimeter, SARAL/AltiKa—have, however, resulted in a significantly lower noise level (e.g. Figure 2). This has helped reveal the small-scale tectonic structures including abyssal hills, small seamounts, and now seesaw propagators. SSPs were evident in older VGG maps (e.g. Matthews et al., 2011), but it is the extra clarity provided by these new data that have revealed their symmetry across the ridges and their similarities with ordinary propagating ridges.

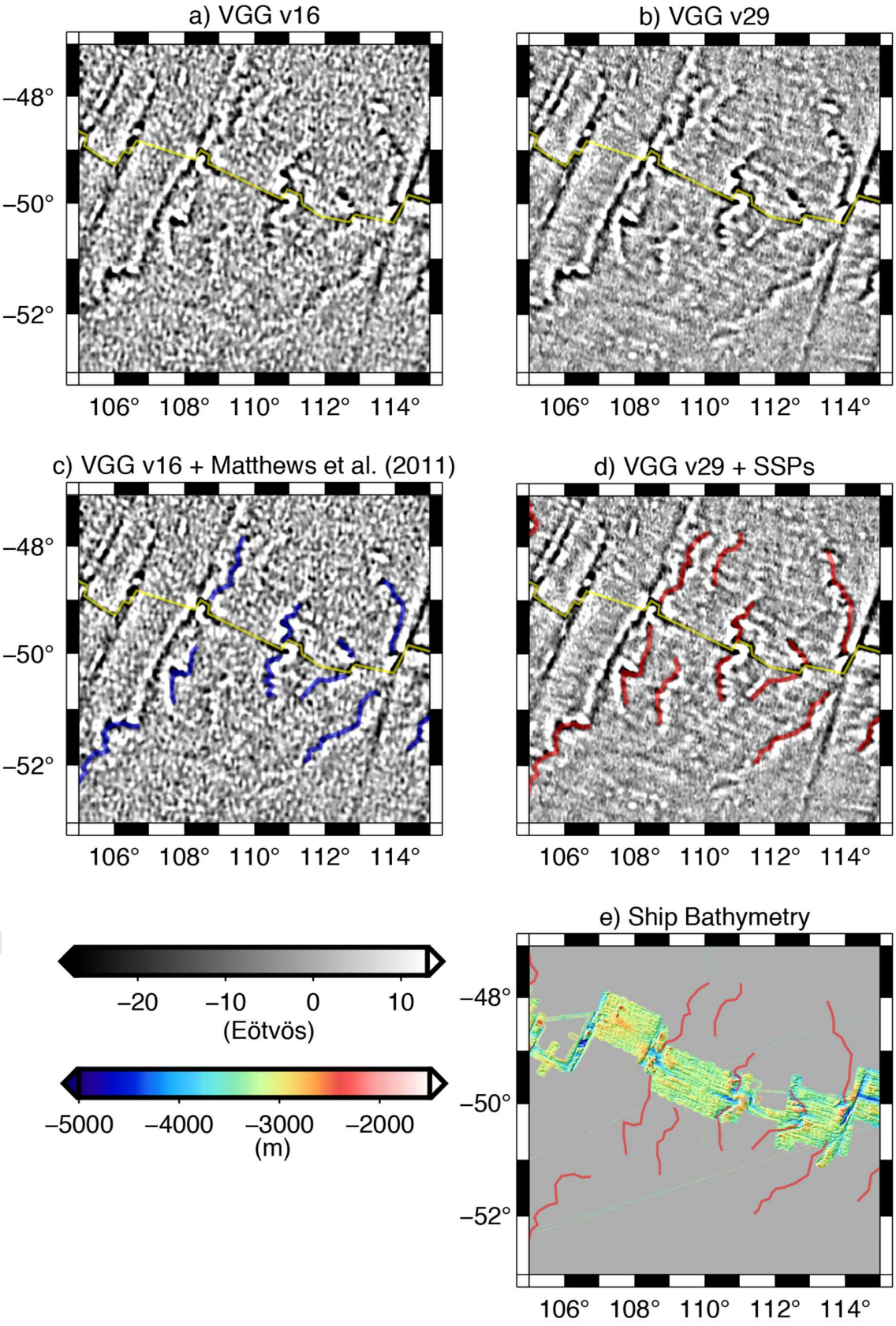

Figure 2. Comparison between (a) VGG v16 (used by Matthews et al., (2011)) and (b) v29 (used in this study). Note the significantly reduced noise level reveals several previously unidentified SSPs and the extra clarity allows for a more confident identification of the traces of others. The yellow lines trace Southeast Indian Ridge. Features identified in Matthews et al. (2011) (as DZs) are shown in (c). Identified SSPs of this study are shown in (d) as red lines, and available shipboard bathymetry in the region is shown in (e) (Cochran and Sempere, 1997). Shipboard data shows high resolution morphology of the propagators near the ridge, and satellite data shows a complex history of propagation. Note the units of Eötvös = 10^{-9} s^{-2}.

2.2 Multibeam bathymetry

Multibeam sonar data provide higher-resolution details of SSP morphology compared to the VGG, thus revealing clearer details of their tectonic histories. However, such data are scarce, particularly away from active ridge axes. Previous studies near the ridge axis include those of, for example: Carbotte et al., (1991), Fox et al., (1991), and Grindlay et al. (1991), who analyzed discontinuities along the South Mid-Atlantic Ridge (MAR); Sempéré et al., (1993), along the north MAR; Cochran and Sempéré (1997) and Goff et al. (1997) along the Southeast Indian Ridge; and more recently Dannowski et al., (2018) and Zheng et al., (2019), who analyzed the behavior of non-transform discontinuities (many of which we consider SSPs), along a section of the North MAR.

In this study, we make use of a publicly available multibeam dataset, recently acquired as part of the search for missing Malaysia Airlines Flight 370 (MH370) by the Governments of Australia, Malaysia and the People's Republic of China (2017) (Geoscience Australia, 2017; Picard et al., 2018). This consists of ~ 279,000 km^2 of multibeam bathymetry data concentrated along a ~180 km wide central swath that runs sub-parallel to the Australian plates flowline in the Southeast Indian Ocean (SEIO). A portion of these data are shown in Figure 3, where the search path fortuitously mapped two off-axis SSPs, providing the best record of off-axis SSP morphology to date. We use these data to assess SSP morphology as well as determine the effective elastic thickness of the lithosphere (T_E) associated with these features by analyzing them in conjunction with satellite-derived free-air gravity anomalies.

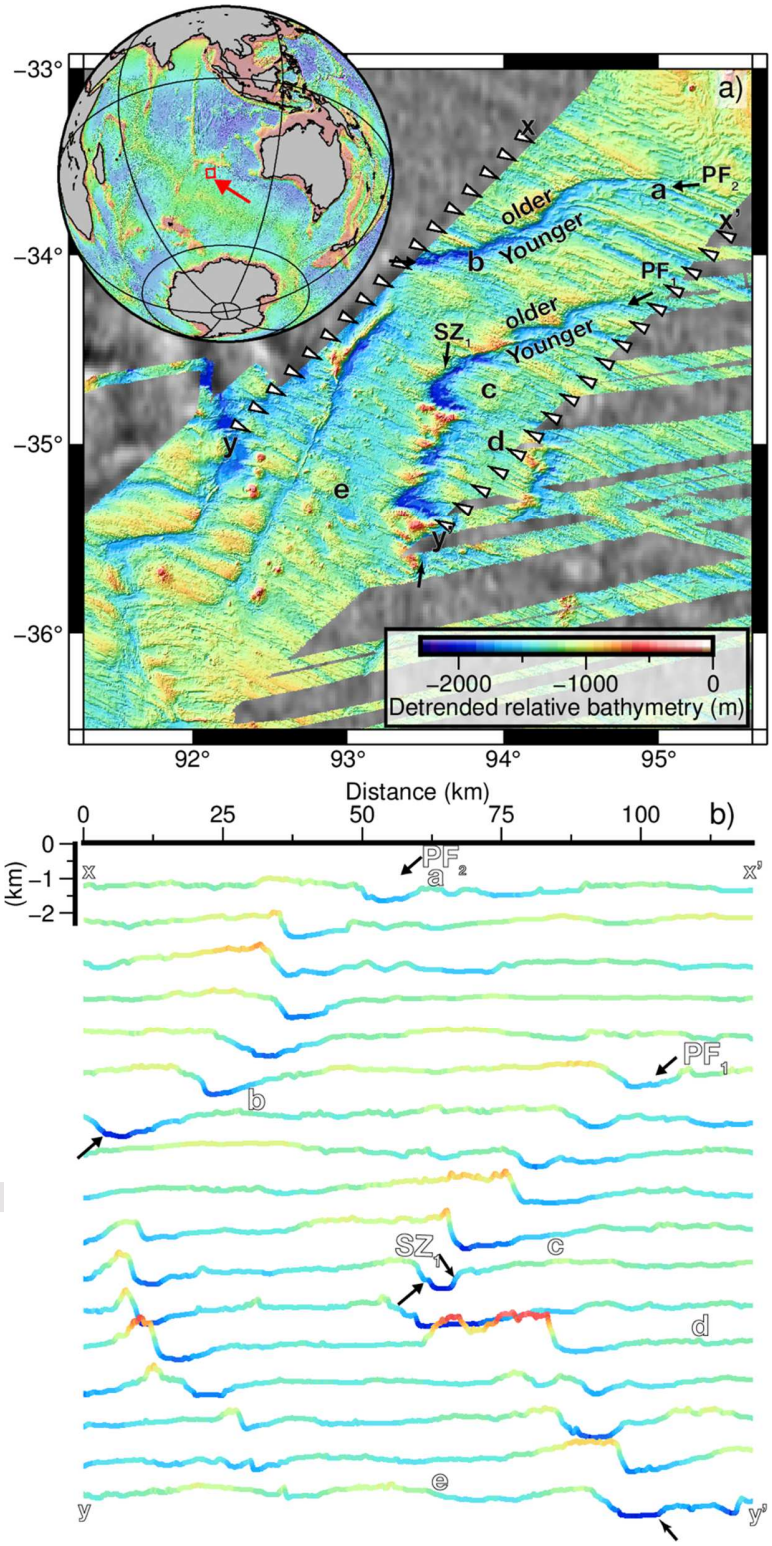

Figure 3. (a) Multibeam bathymetry over two off-axis SSPs collected in the Southeast Indian Ocean as part of the search for missing flight MH370 (GA, 2017). Note, to highlight the morphology of the SSPs with respect to their surroundings, these data have been detrended to remove the regional deepening with age trend and plotted relative to the shallowest depth within the mapped region. Mapping of the northernmost SSP captured only the outer pseudofault (PF_2) section, while mapping of the southern SSP reveals both outer pseudofault (PF_1) and subsequent sheared zone (SZ_1), which formed following a reversal in propagation direction. White triangles indicate the locations of the profiles shown in (b). The inset globe shows the location of (a) (red box). (b) Bathymetric profiles showing the gross morphology of the two outer pseudofaults (PF) and a sheared zone (SZ). The letter labels match the locations shown in (a). Note the SSP bathymetric depressions are ~ 10-15 km wide with amplitudes up to ~ 1 km relative to their flanks.

3. Results and Discussion

3.1 Identification and digitization of SSPs

SSPs appear as continuous Eötvös lows in the VGG, typically with amplitudes of ~20 Eötvös relative to their surroundings. They trend dominantly in the direction of spreading but with an oblique component that flips polarity ("seesaws") typically on timescales of a few million years (e.g. Figure 1). SSPs that are presently "active" can be traced to their associated ridge discontinuities, and like unidirectional propagators, fracture zones and abyssal hills, are approximately symmetric about the ridge axis. The signal of off-axis "fossil" SSPs is similar to those found near the ridges, and in some cases, appears as prominent as fracture zones, even thousands of kilometers from the ridge axis (Figure 4).

In order to catalog both active and fossil SSPs globally, we used a variety of data including the satellite derived VGG and free-air gravity anomalies (Sandwell et al., 2019), multibeam bathymetry (where available) and earthquake locations (Engdahl et al., 1998). We also re-digitized those MOR segments in close proximity to SSPs (and transform faults) from traces previously published by Sandwell & Smith (2009). Using the VGG grid, our new picks of the ridge axis have inflection points in locations of VGG lows. This required relaxing the ridge/transform orthogonality adhered to in the Sandwell & Smith (2009) study and only transforms which have clear fracture zone extensions were included.

We began our SSP cataloguing by modifying the interpretations of features Matthews et al., (2011) made by analyzing VGG v16. An identical set of digitized features was also included in the supplemental materials of (Wessel et al., 2015) as part of the GSFML database. In their analysis, these features were classified as "discordant zones". The "discordant zone" label has not seen use in recent literature, and some features identified by Matthews et al. (2011) have been called simply NTDs and interpreted as propagating ridges (e.g., Dannowski et al., 2018; Zheng et al. 2019). Because of the complex temporal and spatial propagation patterns these features exhibit, we feel "seesaw propagator" is an appropriate and descriptive term. Since these original picks were made, the improvement in the quality of the VGG data has revealed many more SSP traces and subtle reversals in polarity that were previously unidentifiable (Figure 2). We use 224 features (112 pairs) identified by Matthews et al. (2011), many of which we have modified to fit new VGG maps. We identify an additional 146 features (73 pairs), for a total 370 SSPs (185 pairs), most of which are located in the Atlantic and Indian Ocean basins.

Our approach for digitizing SSPs followed two main rules: First, because SSPs create bathymetric valleys (e.g. Figure 3), they are always expressed as local Eötvös lows in the VGG, we therefore digitized along the central axes of these lows. Second, both conjugate pairs (i.e., the outer pseudofault and sheared zone) had to be identifiable and symmetric about the spreading axis. For active SSPs, which can be traced from the ridge axis, there is little ambiguity here (e.g. Figure 4e-g). However, for fossil SSPs located off-axis, satisfying this criterion can be difficult. This is particularly a problem for features located on old seafloor, where the signal may be suppressed by the accumulation of sediments and the subsidence of the lithosphere and/or overprinted by other bathymetric fabrics (e.g. Figure 4a-d). Where these ambiguities prevented

the identification of either conjugate feature or where either trace was unclear, we omitted them from our database. Thus, our SSP count and the related statistics may be considered lower bounds. The total length of the digitized SSPs is about 110,000 km; the total length of fracture zones within the same basins is about 340,000 km. Thus, in the slow and intermediate spreading basins, SSPs are about 30% as abundant as fracture zones in the oceanic crust.

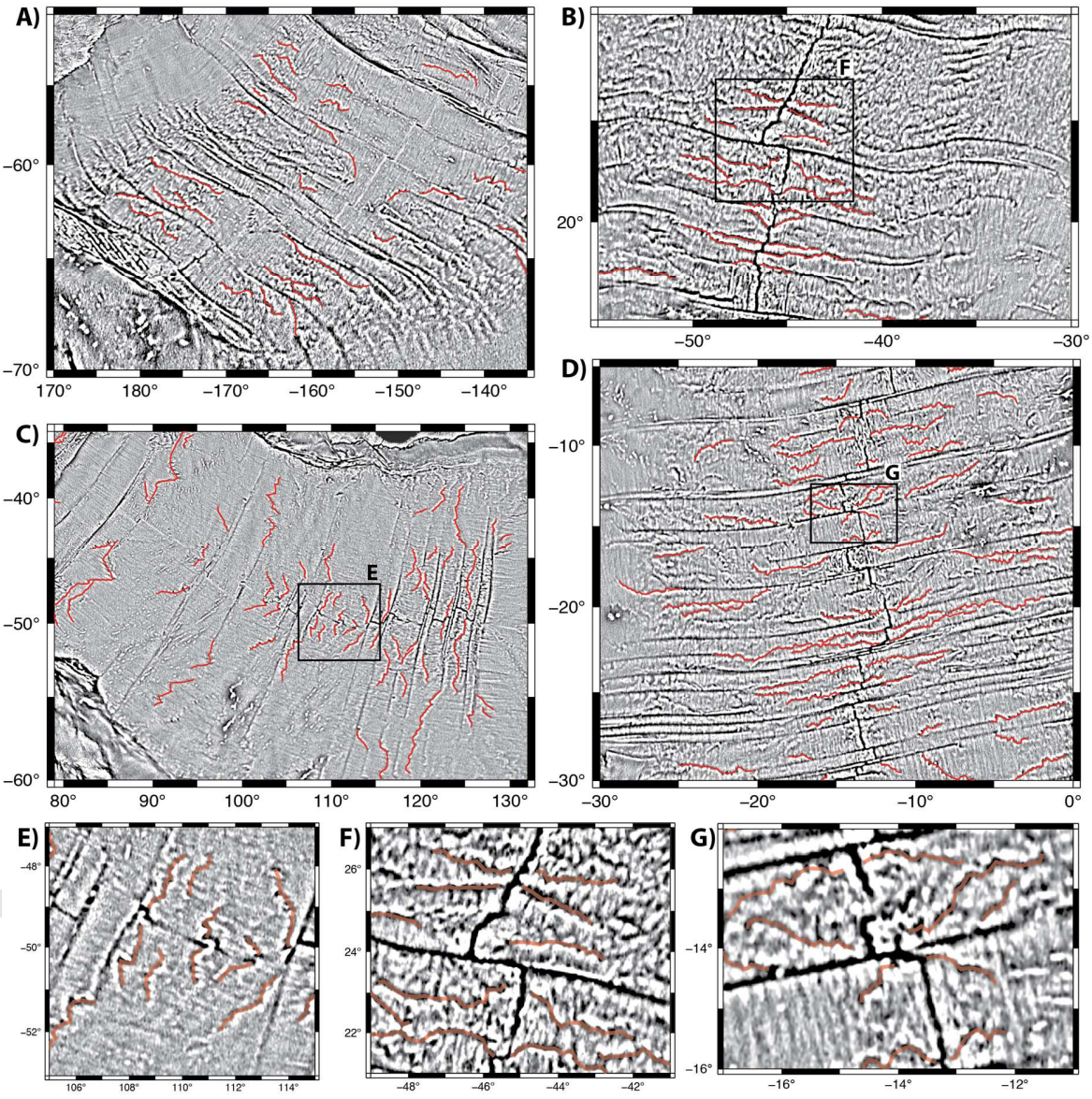

Figure 4. (upper) SSPs in four different basins: (a) South Pacific, (b) North Atlantic, (c) Southeast Indian, (d) South Atlantic. SSPs form in pairs symmetric about the spreading ridge and can be identified by their symmetry even in old oceanic crust. Virtually all active SSPs occur along axial valley ridge morphologies (VGG lows). (lower) Zoom of three areas along spreading

ridges where propagators are presently propagating in both directions within single or nearby segments.

3.2 Spreading rates and age offsets of SSPs

In order to better understand the relationships between the distribution of SSPs and transform faults with respect to seafloor spreading rate and the age offset across a given ridge discontinuity, we analyzed our new SSP and transform fault catalogue in conjunction with the global age and spreading rate grids of Muller et al., (2016). To obtain the spreading rate at the time of formation of each SSP, we computed the centroid and length of each digitized SSP polyline segment and sampled the centroid on the global spreading rate grid. This spreading rate distribution with respect to half spreading rate (binned at 2 mm yr^{-1}) is shown in Figure 5a. The distribution peaks at 22 mm yr^{-1} half-rate and drops to zero at both ultraslow (< 10 mm yr^{-1}) ridges and fast ridges (> 40 mm yr^{-1}). The upper spreading rate limit is broadly coincident with the transition range in ridge topography from axial valley to axial high. This limit in the distribution doesn't necessarily suggest that SSPs only occur at axial valley-type ridges, but that the relief created in the seafloor at axial valley SSPs is sufficient enough to be visible in the satellite VGG data. Due to upward continuation, bathymetric features with a smaller spatial wavelength (<12 km) and/or less relief cannot be reliably detected in satellite VGG (Sandwell et al., 2019). Pseudofaults at fast-spreading ridges are often harder to observe in the bathymetry (e.g. Cormier et al., 1994; Hey et al., 1995). Similarly, bathymetric variations created by NTD's at fast spreading ridges are subtle or indistinguishable from the surrounding seafloor, although these have been identified by high-resolution mapping of variations in crustal thickness (Boulahanis et al., 2020).

To determine the distribution of transform faults and SSPs with respect to age offset, we measured the transform fault and SSP ridge offset lengths and divided by the current half spreading rate. Since active SSPs are primarily found along the Mid Atlantic Ridge (MAR) and the Southeast Indian Ridge (SEIR), we restricted this analysis to these ridges. These two distributions are shown in Figure 5b. SSPs have a maximum age offset of about 2.5 Ma, while transform faults usually have age offsets greater than 2 Ma; these results are consistent with other studies of non-transform offsets (Macdonald et al., 1988; Macdonald et al., 1992; Grindlay et al., 1991). Since depth-integrated lithospheric strength increases with the age of the lithosphere, we speculate that seesaw propagation is not possible when the age offset is greater than about 2.5 Ma. This is consistent with the inferences of Grindlay et al., 1991, who suggested that a mechanical transition from non-rigid to rigid deformation occurs in MOR discontinuities when the segment offset length is larger than ~ 30 km.

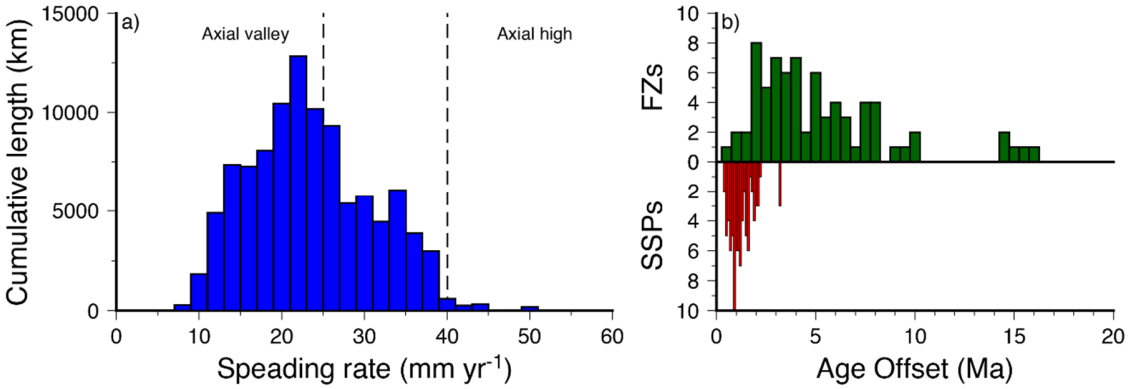

Figure 5. (a) The distribution of SSPs with respect to half spreading rate. The upper limit of < 25–40 mm yr^{-1} is coincident with the transition from axial valley to axial ridge morphology (when the transition is expressed as a function of spreading rate only) (Small and Sandwell, 1994; Chen and Morgan, 1990; Malinverno, 1991). We see no SSPs at ultraslow ridges (< 10 mm yr^{-1})—in these environments (Southwest Indian ridge or the Arctic), neither the ridge segmentation or the off-axis tectonic fabrics are well developed. (b) Distribution of lithospheric age offset across active discontinuities along the Mid-Atlantic Ridge and Southeast Indian Ridge. SSPs (red) generally have offsets less than 2.5 million years, whereas transform faults (green) usually have larger age offsets.

3.3 Morphology and isostatic compensation of SSPs

We investigate the detailed morphology and isostatic compensation of off-axis SSPs using high-resolution multibeam bathymetric data collected as part of the search for the missing Malaysia Airlines Flight 370 (MH370). The detailed bathymetry for one complete "seesaw" propagation cycle of a fossil SSP (PF_1 and SZ_1), as well as an additional outer pseudofault (PF_2) from another SSP is shown in Figure 3. The bathymetry has been detrended to remove the effect of the seafloor subsidence with age and reveals that both outer pseudofault valleys are ~ 15–20 km wide and exhibit a deepening of several hundred meters over age. They also exhibit pronounced bathymetric highs on the older sides (in front of the direction of propagation) and broad lows towards the younger side. This high-low morphology is also evident in the sheared zone (SZ_1), although the relationship is reversed (i.e. the bathymetric highs occur on the younger side). Based on this analysis, as well as the recent multibeam analysis by Zheng et al., (2019), we propose that SSPs typically form 1-2 km of relief, similar to oceanic fracture zones that form at the same spreading rate. As the overall length of the SSPs is about 30% of the length of fracture zones, they therefore represent a major component of global seafloor roughness. Rough seafloor can generate substantial internal tides as tidal currents interact with topography, and internal tides contribute to mixing in the deep ocean (Garrett, 2003). How much SSP topography, independent of abyssal hills and fracture zones, affects internal tide generation remains to be studied.

As shown above, the age offsets across SSPs forming today are less than about 2.5 Ma which suggests that all SSPs form on very young lithosphere where the bathymetric troughs of the SSPs

is locally compensated by thinner than normal crust (Zheng et al., 2019). In contrast, transform faults usually have larger age offsets and therefore much of the topography is formed on lithosphere that is somewhat older (2-10 Ma). This difference in age should be evident as a difference in the effective elastic thickness (T_e), a proxy for lithosphere strength that usually increases with age as the plate cools. To test this hypothesis, we modelled the free-air gravity anomalies expected from the MH370 bathymetry and its isostatic compensation using a thin elastic plate flexure model. Two areas were selected (i.e., (a) and (b) in Figure 6); the SSP area (a) has a seafloor age of ~ 22–35 Ma while the Geelvinck fracture region (b) has a seafloor age of ~11–20 Ma. We adopted a forward modelling approach (e.g. Watts et al., 2006), and compared the modelled gravity with the satellite-derived gravity. The steps below outline our method using GMT (Wessel et al., 2019) which we applied for a range of constant T_e values between 0–30 km:

1. High-pass filter the bathymetry (SRTM15+V2, Tozer et al., 2019) and free-air anomalies (Sandwell et al., 2019) to remove the long wavelength component from the gravity field which is not associated with isostatic compensation of the seafloor features, such as deep mantle dynamics and fully compensated bathymetry (e.g. Watts & Moore, 2017). These filters were applied to spherical harmonic representations of the data using a cut-off wavelength of ~ 400 km (degree n=100) cosine tapered to ~ 571 km (degree n=70).
2. For a uniform plate, calculate the Moho topography required to compensate for the bathymetry load given a prescribed T_e value.
3. Calculate the gravity anomaly produced by the bathymetry and its isostatic compensation (i.e., the Moho topography) using the method of Parker (1973), expanding the series to four terms. For these calculations, standard parameter values were used, as outlined in the table inset of Figure 6. In order to avoid edge effects, the root-mean-square (RMS) misfit calculations were restricted to multibeam bathymetry coverage within the areas (a) and (b) shown in Figure 6, while the calculations were performed for regions extending ~ 300 km beyond these using predicted bathymetry from Tozer et al., (2019).
4. Compute the RMS misfit between the calculated and observed gravity anomalies.

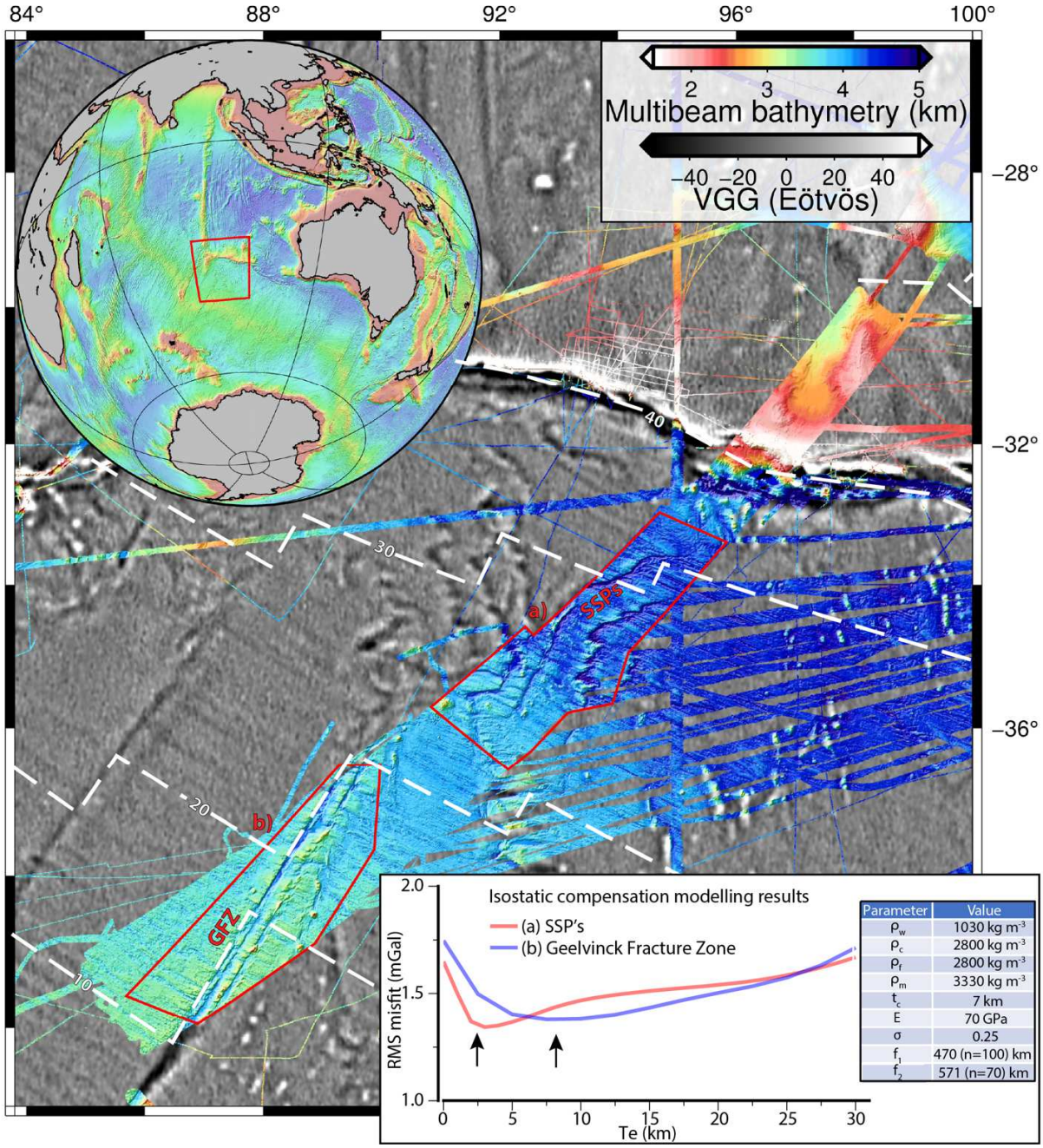

Figure 6. Multibeam bathymetry acquired during the search for missing flight MH370 (GA, 2017) overlain on the regional VGG grid. Red boxes show the areas used for RMS calculations in the isostatic modelling of the SSPs (a) and Geelvinck Fracture Zone (b). Dashed lines = seafloor age contours (Ma) from Muller et al., (2016). The globe Inset shows the location of the main map (red box). The box inset shows RMS misfits for isostatic compensation models calculated using the given T_e values. Values for other physical parameters used for the modelling are listed in the inset table (ρ_w – water density; ρ_c – crustal density; ρ_f – infill density; ρ_m – mantle density; t_c – crustal thickness; E – Young's modulus; sigma – Poisson's ratio; $f_{1,2}$ – filter

parameters). The black arrows indicate the best-fit T_e values for each region (i.e. 3 km for the SSPs and 8 km for the Geelvinck Fracture Zone). Note the units of Eötvös = 10^{-9} s^{-2}.

The results are shown in the inset of Figure 6. For both areas, the RMS misfit versus T_e has a broad minimum reflecting a mixture of tectonic processes in each region. Nevertheless, the best-fit T_e for the SSPs of 3 km is significantly less than the 8 km for the Geelvinck Fracture Zone. We interpret the low T_e value for the SSPs as reflecting the "frozen-in" strength of the lithosphere at the time of formation. That is, these features formed across a narrow discontinuity on very thin and weak lithosphere near the ridge axis. The bathymetric troughs are associated with thin crust and thus shallower than normal mantle in agreement with the analysis of Zheng et al., (2019). In contrast, the value across the Geelvinck Fracture Zone—which separates seafloor with a much larger age contrast (~ 5 Ma)—reflects the averaged signal of the time-dependent flexural compensation required to maintain this feature (e.g., Sandwell & Schubert, 1982). This involves the flexure of older, and hence stronger lithosphere, which is reflected in the larger T_e value.

3.4 Symmetry of SSPs and new data type for reconstructions

One of the important characteristics of SSPs is that the symmetric kinks in their off-ridge traces provide a new type of data that can be used to refine detailed plate reconstructions. Moreover, it is not just the kinks in the traces, but the overall shape of the traces that should be symmetrical about a spreading ridge (assuming purely symmetric spreading). We tested this hypothesis using four prominent SSP traces along the SEIR. For each pair, we approximated a pole of opening for that age range by fitting a pole to a nearby fracture zone. We measured the deviation of the SSP trace from the small circle of opening, and plotted this deviation against the age of the plate as sampled from the Muller et al., (2016) age map (Figure 7). The shapes of the SSP deviations match well in this coordinate system—which verifies that the "excursions" from the small circle path are age-concurrent for each SSP pair. There are, however, some incongruities that are not so easily explained. Additionally, by plotting these data in this coordinate system, we can easily see the approximate rate of propagation along a ridge axis and how abruptly it may change.

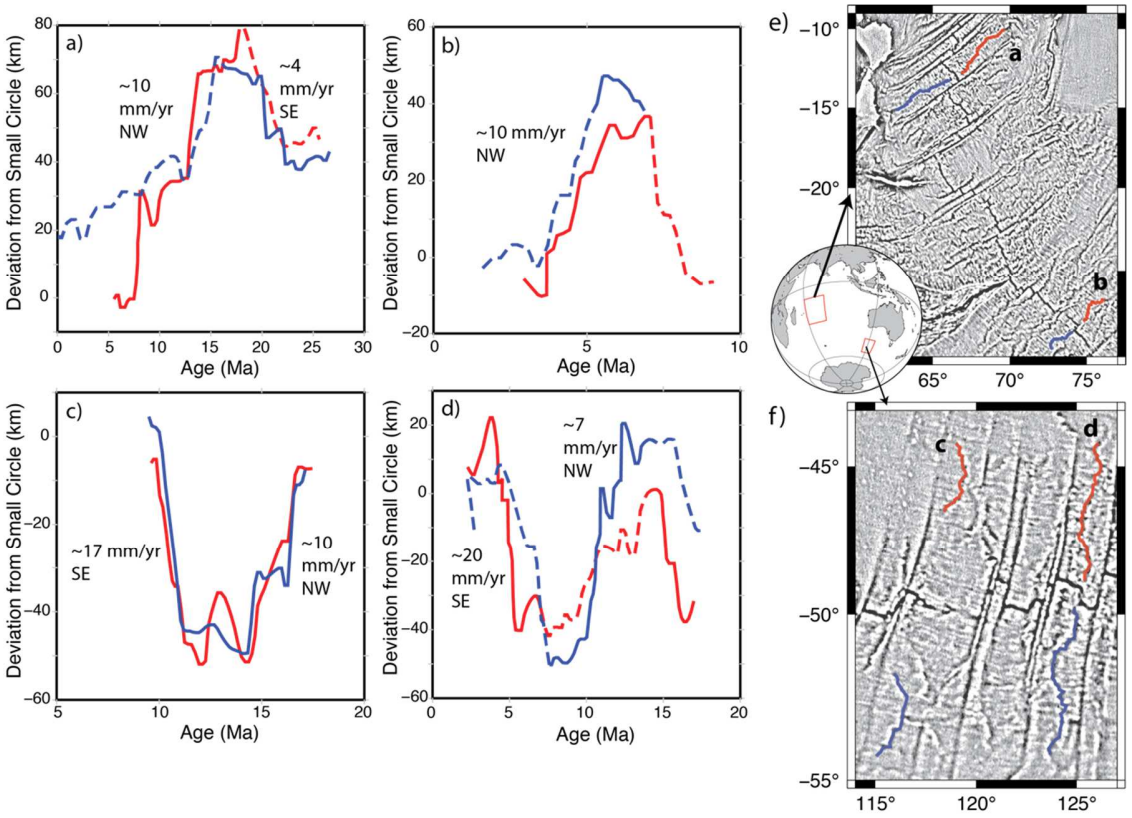

Figure 7. Four prominent SSP pairs in in the Southeast Indian Ocean and their deviation from the small circle of plate spreading with respect to age (red – Australian Plate, blue – Antarctic Plate (African Plate for a). A solid line indicates the outer pseudofault branch of the segment, and a dashed line indicates the sheared zone (no distinction is made for (c) where neither the sense of offset nor morphology is clear). Location maps for the SSPs are shown in (e-f). The match of the deviations across the ridge reveals their symmetry. Mismatches may be due to asymmetric spreading, small errors in the age grid, and/or errors in identifying the center of the relatively wide sheared zones.

3.5 Assessment of SSP propagation models

Several hypotheses have been proposed to explain unidirectional ridge propagation. Dannowski et al., (2018) recently reviewed these mechanisms, which include: (1) reorientation of the ridge axis in response to large-scale changes in plate motion (e.g., Hey & Wilson, 1982; Lonsdale, 1985) (2) propagation down a regional topography or gravity gradient (e.g. Phipps-Morgan & Sandwell, 1994) or as a result of asthenospheric flow (West et al., 1999); and (3) propagation in response to hotspot volcanism (Hey & Vogt, 1977; Hey et al., 1980; Phipps-Morgan and Parmentier, 1985). These hypotheses are not exclusive and they are often invoked together. Importantly, each of these processes would produce predictable patterns in SSP behavior that are testable. Figure 8 shows SSPs in the South Atlantic and uses this basin as a case study for qualitative testing of these hypotheses. SSPs that intersect the ridge and have a clear propagation direction are marked as arrows above the profile plots (Figures 8b-d).

Hypothesis (1) predicts that when there is a change in plate motion, all active ridges should propagate uniformly toward the pole of plate rotation during clockwise changes in spreading direction and, conversely, away from the pole of opening during anticlockwise changes (Lonsdale, 1985), such that, the direction of propagation would be the same for all SSPs along a given isochron since the pole change is a simple function of age. Clearly this does not explain the observed distribution of active SSPs along the MAR, which show many reversals in propagation direction along the ridge. Additionally, we have estimated ages at SSP "inflection points" where the direction of propagation changes and found no clustering of these changes around plate reorganization events (e.g. Lonsdale, 1985) and instead see a more random distribution of changes through time (Figure 8f).

Hypothesis (2) predicts that all the propagators move down a regional topography or gravity gradient. To test this hypothesis, we low-pass filtered both the gravity and the bathymetry with 0.5 gain at 160 km wavelength as shown in Figure 8a,c. The filtered gravity and bathymetry at the ridge axis are shown as red curves in Figure 8b,d. The propagators are marked as black dots and the arrows show the direction of propagation. There is no clear correlation between currently active SSPs and the regional bathymetric and gravity gradients. Moreover, there are numerous examples of active propagation in the up-gradient direction, suggesting this process is not the primary driver of this style of ridge propagation. Propagation driven by asthenospheric flow, such as in West et al., (1999), has a similar pattern of regionally coherent propagation, which is not observed.

Hypothesis (3) predicts that the propagators move away from the upwelling hotspots. Three South Atlantic hotspots are marked as black dots in Figure 8a,c. Although it is difficult to rule out an influence of hotspot activity on propagation entirely, it can be seen from the widespread distribution of SSPs relative to the scarce existence of hotspots, that forces generated by these features are also unlikely to be primary drivers in most cases.

We conclude that the processes proposed to explain unidirectional ridge propagation are, alone, not capable of accounting for the seesaw behavior of SSPs. It therefore appears that a driving mechanism operating on a local scale is more likely. We speculate that SSP propagation may occur as a response to a dynamic magma delivery system, in which, complex upward transport of material from a magma source (e.g. Sempere et al., 1993; Michael et al., 1994; Gente et al., 1995; Tucholke et al., 1997; Martinez and Hey, 2017; Dannowski et al., 2018) causes ridge propagation away from the magma foci. Figure 8a shows that several, but not all, active SSPs near the ridge axis are propagating away from local positive anomalies, which we interpret as representing present day local magma upwellings. Depending on the time scales of such local magma "pulses," they may be capable of producing the propagation patterns we observe. Moreover, local curvature of the spreading ridge topography may reflect these processes. At slow-spreading axial valleys, we see high curvature in general. However, this remains purely conceptual, and we cannot, at this time, comment on the true nature of sub-axial magma chambers. Ultimately, testing this hypothesis must involve dedicated 3D imaging of a slow-spreading axial magma system beneath a system of active SSPs.

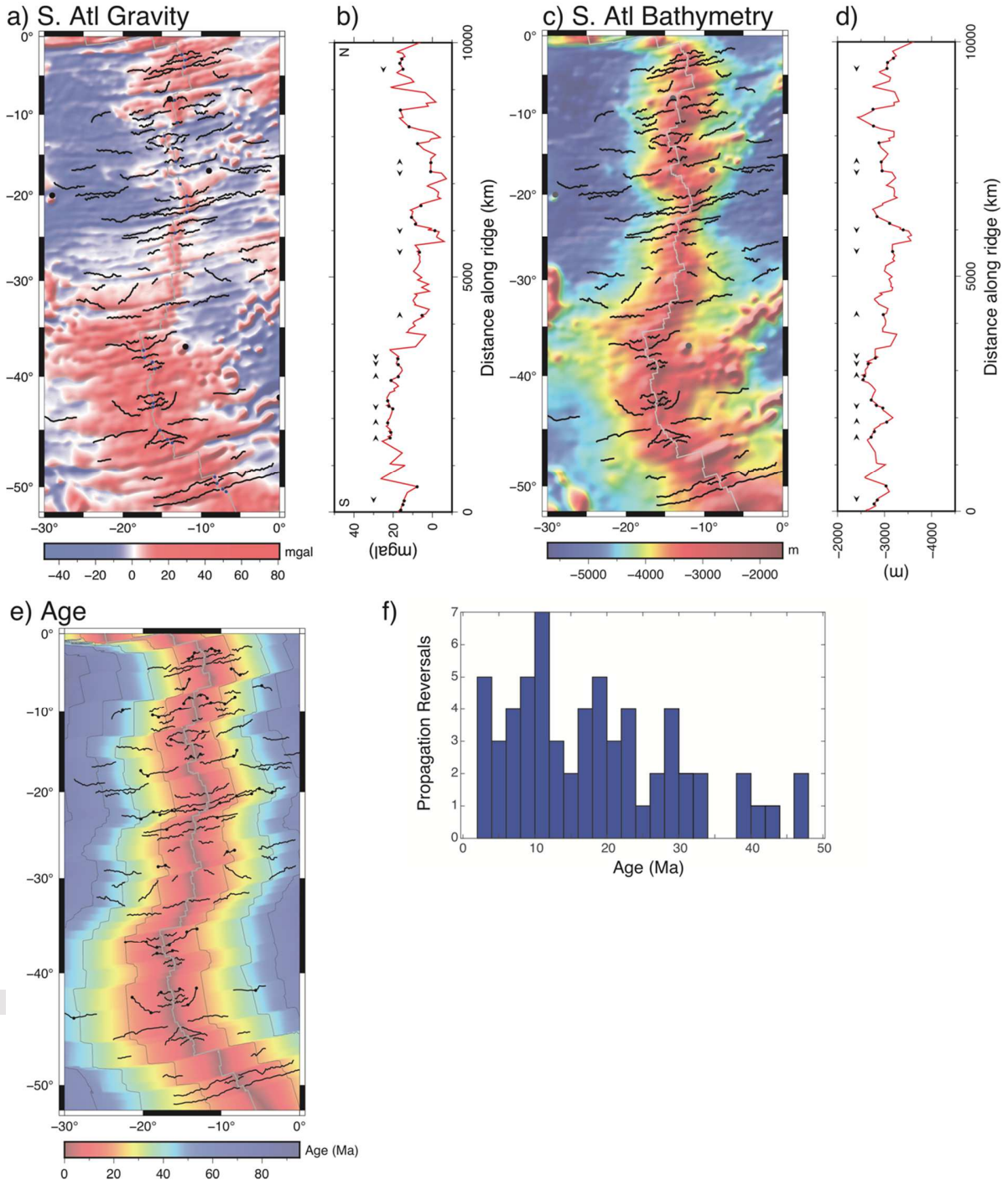

Figure 8. (a) Low-pass filtered gravity anomaly with present-day ridge axis (gray) and digitized SSPs (black). (b) The depth versus distance along ridge shows regional gravity gradients, and the propagation direction at intersection points of SSPs and the ridge are shown by small arrows. (c-d) Same as (a-b) except for low-pass filtered bathymetry (Tozer et al., 2019). (e) The Muller et al., (2016) age grid and interpreted SSPs. Within this region, we selected points on SSPs that indicated changes in propagation direction or major change in rate and sampled these points on

the age grid. (f) Shows the distribution of these changes through time. There isn't an obvious clustering of the propagation changes with time, but there is a noticeable decrease—this is due to our conservative selection of SSPs and the propagation changes which aren't as clear in older crust.

4 Conclusions

In this study we have documented the global distribution of seesaw propagators, analyzed their distribution and nature with respect to tectonic setting and tested mechanisms to explain their formation and behavior. We draw the following conclusions:

- Seesaw ridge propagation is a ubiquitous phenomenon that occurs at slow and intermediate spreading ridges (i.e., half spreading rates between 10-40 mm yr^{-1}). The total length of the identified seesaw propagators is about 30% of the total length of fracture zones within the slow and intermediate spreading basins.
- SSPs form almost exclusively at discontinuities with lithospheric age contrasts less than ~ 2.5 Ma. This likely reflects a rheological threshold, whereby only young and weak lithosphere allows for "non-rigid" SSP behavior (Grindlay et al., 1991).
- Seesaw propagation results in W-shaped bathymetric valleys ~ 10–20 km wide and ~ 1-2 km deep with respect to the surrounding seafloor. These valleys are asymmetric with steep slopes on the older side of outer pseudofaults and broad shallower slopes towards the younger side. This morphology is mirrored for the sheared zones.
- The elastic thickness of two fossil SSPs was found to be very low (~ 3 km) confirming they formed on hot, young lithosphere near the ridge axis.
- Because SSPs are symmetric about ridge axes, the inflection points (where they reverse direction) of fossil SSPs can be used to improve the accuracy of plate reconstructions as these points must meet at the ridge axis when reconstructed to the time of formation of the given SSP pairs.
- Processes previously proposed to explain unidirectional ridge propagation appear unable to account for SSP behavior. We therefore speculate that local spatial and temporal variations in magma supply may provide the driving forces required to produce SSPs (e.g., Zheng et al., 2019).

Acknowledgments, Samples, and Data

The authors thank ESA, NASA, ISRO and CNES for the open policy and access to the raw waveform data on all the altimeter datasets. We extend our thanks to the reviewers who helped us improve the focus and presentation of this work. This work was supported by the NASA SWOT program (NNX16AH64G) and the Office of Naval Research (N00014-17-1-2866). The Generic Mapping Tools (Wessel, et al., 2019) were used extensively in data analysis and to generate figures. The latest vertical gravity gradient products can be found at ftp://topex.ucsd.edu/pub/global_grav_1min/, and the SRTM15+V2 bathymetry (Tozer et al., 2019) can be found at ftp://topex.ucsd.edu/pub/srtm15_plus/. Cryosat-2 waveform data can be found at https://science-pds.cryosat.esa.int/. Jason-1/2 and SARAL/AltiKa waveform data can be found at https://www.aviso.altimetry.fr/en/data/products/sea-surface-height-

products/global/waveforms.html. MH370 search bathymetry can be found at https://portal.ga.gov.au/persona/marine.

References

Boulahanis, B., Carbotte, S. M., Huybers, P. J., Nedimović, M. R., Aghaei, O., Canales, J. P., & Langmuir, C. H. (2020). Do sea level variations influence mid-ocean ridge magma supply? A test using crustal thickness and bathymetry data from the East Pacific Rise. *Earth and Planetary Science Letters*, *535*, 116121.

Briais, A., & Rabinowicz, M. (2002). Temporal variations of the segmentation of slow to intermediate spreading mid-ocean ridges 1. Synoptic observations based on satellite altimetry data. *Journal of Geophysical Research: Solid Earth*, *107*(B5), ECV-3.

Carbotte, S.M., Smith, D.K., Cannat, M. and Klein, E.M., (2015). Tectonic and magmatic segmentation of the Global Ocean Ridge System: a synthesis of observations. Geological Society, London, Special Publications, 420(1), pp.249-295.

Carbotte, S., Welch, S. M., & MacDonald, K. C. (1991). Spreading rates, rift propagation, and fracture zone offset histories during the past 5 my on the Mid-Atlantic Ridge; 25°-27°30′ S and 31°-34°30′ S. *Marine Geophysical Researches*, *13*(1), 51–80. https://doi.org/10.1007/BF02428195

Chen, Y. J., & Morgan, W. J. (1990). Rift Valley/No Rift Valley Transition at Mid- Ocean Ridges. Journal of Geophysical Research, 95(B11), 17.571–17.581.

Cochran, J. R., & Sempéré, J. C. (1997). The Southeast Indian Ridge between 88 E and 118 E: Gravity anomalies and crustal accretion at intermediate spreading rates. *Journal of Geophysical Research: Solid Earth*, *102*(B7), 15463-15487.

Cormier, M.H., Macdonald, K.C., (1994). East Pacific Rise 18–19S: asymmetric spreading and ridge reorientation by ultrafast migration of axial discontinuities. J. Geophys. Res.99, 543–564

Dannowski, A., I. Grevemeyer, J. Phipps Morgan, C. R. Ranero, M. Maia, and G. Klein (2011). Crustal structure of the propagating TAMMAR ridge segment on the Mid-Atlantic Ridge, 21.5°N, Geochem. Geophys. Geosyst., 12, Q07012, doi:10.1029/2011GC003534

Dannowski, A., Morgan, J. P., Grevemeyer, I., & Ranero, C. R. (2018). Enhanced Mantle Upwelling/Melting Caused Segment Propagation, Oceanic Core Complex Die Off, and the Death of a Transform Fault: The Mid-Atlantic Ridge at 21.5°N. *Journal of Geophysical Research: Solid Earth*, *123*(2), 941–956. https://doi.org/10.1002/2017JB014273

Dunn, R. A. (2015). Crust and Lithospheric Structure - Seismic Structure of Mid-Ocean Ridges (Vol. 1). Elsevier B.V. Retrieved fromhttp://dx.doi.org/10.1016/B978-0-444-53802-4.00011-7doi: 10.1016/B978-0-444-53802-4.00011298-7

Engdahl, E. R., R. VanderHilst, and R. Buland (1998). Global teleseismic earthquake relocation with improved travel times and procedures for depth determination. IBull. Seismo. Soc. Am., 88:722–743.

Fox, P. J., Grindlay, N. R., & MacDonald, K. C. (1991). The Mid-atlantic Ridge (31°S-34°30′S): Temporal and spatial variations of accretionary processes. *Marine Geophysical Researches*, *13*(1), 1–20. https://doi.org/10.1007/BF02428193

Garrett, C. (2003). Internal tides and ocean mixing. *Science*, *301*(5641), 1858-1859.

Geoscience Australia 2017. MH370 Search Phase 1 Raw and Processed datasets. Geoscience Australia, Canberra. http://dx.doi.org/10.4225/25/595d7744b71e2

Grindlay, N. R., Fox, P. J., & Macdonald, K. C. (1991). Second-order ridge axis dis- continuities in the south Atlantic: Morphology, structure, and evolution. Ma- rine Geophysical Researches, 13(1), 21–49. doi: 10.1007/BF02428194

Hey, R. (1977). A new class of ”pseudofaults” and their bearing on plate tecton- ics: A propagating rift model. Earth and Planetary Science Letters, 37(2), 321–325. doi: 10.1016/0012-821X(77)90177-7

Hey, R. (2001). Propagating Rifts and Microplates. Encyclopedia of Ocean Sciences, 597–605. doi: 10.1016/B978-012374473-9.00095-3

Hey, R., Duennebier, F. K., & Morgan, W. J. (1980). Propagating rifts on midocean ridges. Journal of Geophysical Research: Solid Earth, 85(B7), 3647–3658.

Hey, R., Kleinrock, M., Miller, S., Atwater, T., & Searle, R. (1986). Sea beam/deep-tow investigation of an active oceanic propagating rift system, galapagos 95.5 w. Journal of Geophysical Research: Solid Earth, 91(B3), 3369–3393.

Hey, R.N., P.D. Johnson, F. Martinez, J. Korenaga, M.L. Somers, Q.J. Huggett, T.P. LeBas, R.I. Rusby, and D.F. Naar (1995). Plate boundary reorganization at a large-offset, rapidly propagating rift, Nature, 378, 167-170

Hey, R.N. and P.R. Vogt (1977). Spreading center jumps and sub-axial asthenosphere flow near the Galapagos hotspot, Tectonophysics, 37, 41-52

Hey, R.N. and D.S. Wilson (1982). Propagating rift explanation for the tectonic evolution of the Northeast Pacific - The pseudomovie, Earth Planet. Sci. Lett., 58, 167-188

Johnson, H. P., Karsten, J. L., Delaney, J. R., Davis, E. E., Currie, R. G., & Chase, R. L. (1983). A detailed study of the Cobb offset of the Juan de Fuca Ridge: Evolution of a propagating rift. *Journal of Geophysical Research: Solid Earth*, *88*(B3), 2297-2315.

Karson, J. A. (1986). Lithosphere age, depth and structural complications resulting from migrating transform faults. Journal of the Geological Society , 143 (5), 785–788. doi: 10.1144/gsjgs.143.5.0785

Kent, G., Harding, A., & Orcutt, J. (1990). Evidence for a smaller magma chamber beneath the east pacific rise at 9 30 n. Nature, 344(6267), 650.

Korenaga, J. and R.N. Hey (1996) Recent dueling propagation history at the fastest spreading center, the East Pacific Rise, 26° -32°S, J. Geophys. Res., 101, 18023-18041

Langmuir, C. H., Bender, J. F., & Batiza, R. (1986). Petrological and tectonic seg- mentation of the east pacific rise, 5 30–14 30 n. Nature, 322(6078).

Lonsdale, P. (1985). Nontransform offsets of the Pacific-Cocos plate boundary and their traces on the rise flank. Geological Society of America Bulletin, 96(3), 313–327.

Macdonald, K. C. (1982). Mid-Ocean Ridges: Fine Scale Tectonic, Volcanic and Hydrothermal Processes Within the Plate Boundary Zone. Annual Review of Earth and Planetary Sciences, 10(1), 155–190. doi: 10.1146/ annurev.ea.10.050182.001103

Macdonald, K.C., Sempere, J.C., Fox, P.J. and Tyce, R., (1987). Tectonic evolution of ridge-axis discontinuities by the meeting, linking, or self-decapitation of neighboring ridge segments. Geology, 15(11), pp.993-997.

Macdonald, K. C., Fox, P. J., Perram, L., Eisen, M., Haymon, R., Miller, S., . . . Shor, A. (1988). A new view of the mid-ocean ridge from the behaviour of ridge-axis discontinuities. Nature, 335(15).

Macdonald, K. C., Scheirer, D. S., & Carbotte, S. M. (1991). Mid-Ocean Ridges: Discontinuities, Segments and Giant Cracks. Science, 253(5023), 986–994.

Macdonald, K. C., Sempere, J. C., Fox, P. J., & Tyce, R. (1987). Tectonic evolution of ridge-axis discontinuities by the meeting, linking, or self- decapitation of neighboring ridge segments. Geology, 15(11), 993–997. doi: 10.1130/0091-7613(1987)15⟨993:TEORDB⟩2.0.CO;2

Malinverno, A. (1991). Inverse square-root dependence of mid-ocean-ridge flank roughness on spreading rate. *Nature*, *352*(6330), 58-60.

Martinez, F., and R. Hey, (2017). Propagating buoyant mantle upwelling on the Reykjanes Ridge, Earth Planet. Sci. Lett., 457, 10-22, http://dx.doi.org/10.1016/j.epsl.2016.09.057

Matthews, K. J., Mller, R. D., Wessel, P., & Whittaker, J. M. (2011). The tectonic fabric of the ocean basins. Journal of Geophysical Research: Solid Earth, 116(12), 1–28. doi: 10.1029/2011JB008413

McKenzie, D.P., (1986). The geometry of propagating rifts: Earth and Planetary Science Letters, v. 77, p. 176-186.

Menard, H., & Atwater, T. (1969). Origin of fracture zone topography. Nature, 222(5198), 1037–1040.

Michael, P.J., et al., (1994). Mantle control of a dynamically evolving spreading center: Mid-Atlantic Ridge 31–34S. Earth Planet. Sci. Lett. 121, 451–468.

Muller, R. D., Seton, M., Zahirovic, S., Williams, S. E., Matthews, K. J., Wright, N. M., . . . Cannon, J. (2016). Ocean Basin Evolution and Global-Scale Plate Reorganization Events Since Pangea Breakup. Annual Review of Earth and Planetary Sciences, 44(1), 107–138. doi: 10.1146/annurev-earth-060115 -012211

Parker, R. L. (1973). The Rapid Calculation of Potential Anomalies. Geophysical Journal of the Royal Astronomical Society, 31(4), 447–455. doi: 10.1111/j.1365 -246X.1973.tb06513.x

Phipps Morgan, J., & Chen, Y. J. (1993). Magma Injection , Hydrothermal Circulation , and Crustal Flow. Journal of Geophysical Research: Solid Earth, 98, 6283–6297.

Phipps Morgan, J., and Parmentier, E. M. (1985). Causes and rate limiting mechanisms of ridge propagation; A fracture mechanics model: Journal of Geophysical Research, v. 90, p. 8603-8612.

Phipps Morgan, J., & Sandwell, D. T. (1994). Systematics of ridge propagation south of 30 degrees S. Earth and Planetary Science Letters, 121.

Picard, K., Brooke, B. P., Harris, P. T., Siwabessy, P. J., Coffin, M. F., Tran, M., ... & Sullivan, J. (2018). Malaysia Airlines flight MH370 search data reveal geomorphology and seafloor processes in the remote southeast Indian Ocean. *Marine Geology*, *395*, 301-319.

Rea, D.K., Asymmetric seafloor spreading and a nontransform axis offset: The East Pacific Rise 20°S survey area (1978), Geol. Soc. Am. Bull., 89, 836-844

Sandwell, D. T., Harper, H., Tozer, B., & Smith, W. H. (2019). Gravity field recov- ery from geodetic altimeter missions. Advances in Space Research. Retrieved from https://doi.org/10.1016/j.asr.2019.09.011 doi: 10.1016/j.asr.2019 .09.011

Sandwell, D. T., & Schubert, G. (1982). Lithospheric flexure at fracture zones. Jour- nal of Geophysical Research, 87, 4657–4667.

Sandwell, D. T., & Smith, W. H. F. (2009). Global marine gravity from re- tracked Geosat and ERS-1 altimetry: Ridge segmentation versus spreading rate. Journal of Geophysical Research, 114(B1), 1–18. Retrieved from http://www.agu.org/pubs/crossref/2009/2008JB006008.shtml doi: 10.1029/2008JB006008

Schouten, H., & White, R. S. (1980). Zero-offset fracture zones. *Geology*, *8*(4), 175-179.

Sempere, J.-C., Lin, J., Brown, H.S., Schouten, H., Purdy, G.M. (1993). Segmentation and morphotectonic variations along a slow-spreading center: the Mid-Atlantic Ridge (24N–30'N). Mar. Geophys. Res. 15, 153–200.

Sempere, J.-C., Purdy, G., & Schouten, H. (1990). Segmentation of the mid-atlantic ridge between 24 n and 30 40’n. Nature, 344(6265), 427.

Small, C., & Sandwell, D. T. (1989). An abrupt change in ridge axis gravity with spreading rate. Journal of Geophysical Research: Solid Earth, 94(B12), 17383-17392.

Small, C., & Sandwell, D. T. (1994). Imaging mid-ocean ridge transitions with satellite gravity. Geology, 22, 123–126.

Tozer, B., Sandwell, D. T., Smith, W. H. F., Olson, C., Beale, J. R., & Wessel, P. (2019). Global bathymetry and topography at 15 arc sec: SRTM15+. *Earth and Space Science*, *6*(10), 1847-1864.

Tucholke, B.E., Lin, J., Kleinrock, M.C., Tivey, M.A., Reed, T.B., Goff, J., Jaroslow, G.E., (1997). Segmentation and crustal structure of the western Mid-Atlantic Ridge flank, 25°25′–27°10′N and 0–29 m.y. J. Geophys. Res. Solid Earth 102 (B5), 10203–10223.

Watts, A. B., & Moore, J. D. P. (2017). Flexural isostasy: Constraints from gravity and topography power spectra. *Journal of Geophysical Research: Solid Earth*. https://doi.org/10.1002/2017JB014571

Watts, A. B., Sandwell, D. T., Smith, W. H. F., & Wessel, P. (2006). Global gravity, bathymetry, and the distribution of submarine volcanism through space and time. *Journal of Geophysical Research: Solid Earth*, *111*(8), 1–26. https://doi.org/10.1029/2005JB004083

Wessel, P., Luis, J.F., Uieda, L., Scharroo, R., Wobbe, F., Smith, W.H.F. and Tian, D., 2019. The generic mapping tools version 6. Geochemistry, Geophysics, Geosystems.

Wessel, P., & Lyons, S. (1997). Distribution of large pacific seamounts from geosat/ers-1: Implications for the history of intraplate volcanism. Journal of Geophysical Research: Solid Earth , 102 (B10), 22459-22475. Retrieved from https://agupubs.onlinelibrary.wiley.com/doi/abs/10.1029/97JB01588 doi: 10.1029/97JB01588

Wessel, P., Matthews, K. J., Muller, R. D., Mazzoni, A., Whittaker, J. M. Myhill, R., & Chandler, M. T. (2015). Semiautomatic fracture zone tracking. Geochemistry, Geophysics, Geosystems , 16 , 2462–2472. doi: 10.1002/2015GC005853

Wilson, D. S. (1990). Kinematics of overlapping rift propagation with cyclic rift failure. *Earth and Planetary Science Letters*, *96*(3-4), 384-392.

Wilson, J. T. (1965). Transform faults, oceanic ridges, and magnetic anomalies southwest of vancouver island. Science, 150(3695), 482–485.

Zheng, T., Tucholke, B. E., & Lin, J. (2019). Long-term evolution of nontransform discontinuities at the Mid-Atlantic Ridge, 24°N–27°30′N. Journal of Geophysical Research: Solid Earth, 124, 10,023–10,055. https://doi. org/10.1029/2019JB017648